Supporting information

A saddle-shaped *o*-tetraphenylene based molecular semiconductor with high glass transition temperature for perovskite solar cells

Jianan Wang,‡[a] Xinrui Xie,‡[b] Yaohang Cai,[b] Lifei He,[b] Yi Yuan,*[b] Weidong Fei,[a] Lidong Wang*[a] and Peng Wang*[b]

[a] *School of Materials Science and Engineering, Harbin Institute of Technology, Harbin 150001, China*

[b] *State Key Laboratory of Silicon Materials, Department of Chemistry, Zhejiang University, Hangzhou 310028, China*

---

* Corresponding authors.

E-mail addresses: yyuan@zju.edu.cn, wld@hit.edu.cn (L. Wang), pw2015@zju.edu.cn (P. Wang).

‡ These two authors contributed this work equally.

1. Experimental section

1.1. Materials

4,4'-Dimethoxydiphenylamine (98%, Zhengzhou Alfa Chemical Co., Ltd.), tris(dibenzylideneacetone)dipalladium ($Pd_2(dba)_3$, 98%, Energy Chemical), tri-*tert*-butylphosphine tetrafluoroborate ($P(t\text{-}Bu)_3{\cdot}HBF_4$, 98%, Energy Chemical), sodium *tert*-butoxide (NaO(*t*-Bu), 98%, Energy Chemical), tetrakis(triphenylphosphine)palladium ($Pd(PPh_3)_4$, 99%, Energy Chemical), toluene (99%, Sinopharm Chemical Reagent Co., Ltd), tetrahydrofuran (THF, 99%, Sinopharm Chemical Reagent Co., Ltd), titanium diisopropoxide bis(acetylacetonate) (TIACA, 75% in isopropanol, Sigma-Aldrich), acetylacetone (ACAC, 99.0%, TCI), ethanol (99.8%, Aladdin), 1-ethyl-3-methylimidazolium bis(trifluoromethanesulfonyl)imide (EMITFSI, 98%, Energy Chemical), bis(pentamethylcyclopentadienyl)iron (DMFc, 98%, ACROS), ferrocene (Fc, 97%, Aldrich), aluminum oxide (Al_2O_3 nanoparticles, particle size < 50 nm, 20 wt% in isopropanol, Aldrich), polystyrene (PS, average Mw 32,000, Sigma-Aldrich), TiO_2 paste (30NR-D, Greatcell Solar), formamidinium iodide (FAI, 99.0%, Greatcell Solar), methylammonium bromide (MABr, 99.0%, Greatcell Solar), PbI_2 (99.99%, TCI), $PbBr_2$ (99.99%, TCI), CsI (99.0%, TCI), dimethyl sulfoxide (DMSO, 99.9%, Sigma-Aldrich), *N*,*N*-dimethylformamide (DMF, 99.8%, Sigma-Aldrich), 4-*tert*-butylpyridine (TBP, 96%, Sigma-Aldrich), spiro-OMeTAD (≥99.8%, Xi'an Polymer Light Technology Corp.), and chlorobenzene (99.8%, Acros Organics) were purchased and used without further purification. 2,7,10,15-Tetrachlorotetraphenylene (4Cl-OTP),[S1] 4-methoxy-*N*-(4-methoxyphenyl)-*N*-(4-(7-(tributylstannyl)-2,3-dihydrothieno [3,4-*b*][1,4]dioxin-5-yl)phenyl)aniline,[S2] and 4-*tert*-butylpyridinium bis(trifluoromethanesulfonyl)imide (BPTFSI)[S3] were prepared according to the literature methods.

1.2. General instrumentation

^1H and ^{13}C nuclear magnetic resonance (NMR) spectra were recorded on a Bruker AVANCE III 400 MHz NMR spectrometer with the chemical shifts against THF-d_8. High resolution mass spectrum (HR-MS) was obtained with a Bruker UltraflexXtreme MALDI-TOF spectrometer. ATR-FTIR spectra were collected on a Bruker Vector 22 FT-IR spectrometer. The single-crystal XRD measurement was performed at 170 K on a D8 Venture diffractometer (Bruker) and then the single-crystal structure was defined using the SHELXTL software. Detailed refinement parameters are given in the attached single crystal .cif file. The crystallographic datum of OTP-OMeDPA has been deposited to the Cambridge Crystallographic Data Center as supplementary publication no. CCDC-2052553. Cyclic voltammetric measurements were performed with a CHI660C electrochemical workstation (CH Instruments), in connection with a three-electrode electrolytic cell composed of a glassy carbon working electrode, a platinum foil counter electrode, an Ag/AgCl (sat. KCl) reference electrode. Measurements were carried out in a 4 mM solution in anhydrous THF with EMITFSI (0.1M) as the supporting electrolyte. DMFc with a half-wave potential of 0.489 V lower than Fc was added as the internal reference. Highest occupied molecular orbital (HOMO) energy levels were calculated from the onset of oxidation and reduction, respectively. Ultraviolet-visible (UV-vis) absorption spectra were measured with a Cary 8454 spectrophotometer (Agilent Technologies). Differential scanning calorimetry (DSC) was performed with a DSC Q100 V9.7 Build 291 at a heating rate of 10 °C min^{-1} in a flowing nitrogen atmosphere. The samples were firs heated to melt and therefore were cooled to a glassy solid. The glass transition temperature was determined from the second cycle heating curve. The thickness of spin-coated film was measured by a KLA-Tencor D-500 stylus profilometer. X-ray diffraction (XRD) patterns of thin films were measured on a Rigaku D/MAX-2550pc diffractometer, using Cu Kα radiation (λ = 0.15418 nm) operated at 10000 W power (40 kV, 250 mA). UPS data were measured with the ThermoFisher ESCALAB 250Xi instrument. Steady-state PL and time-resolved PL measurement were performed with a Life-Spec-II fluorescence spectrometer. Electrochemical impedance spectroscopies (EIS) were recorded on an AutolabPGSTAT302N electrochemical workstation in the dark by applying a 20 mV voltage perturbation over a series of forward bias, with the frequency range from 1 MHz to 100 Hz. The measured impedance spectra were fitted using the Z-view software (v2.80, Scribner Associates Inc.). Atomic force microscopy (AFM) images were recorded with a Park NX-10. Transmission polarization optical microscope images were recorded on a SDPTOP CX40P system.

1.3. Synthesis of $N^2,N^2,N^7,N^7,N^{10},N^{10},N^{15},N^{15}$-octakis(4-methoxyphenyl)tetraphenylene-2,7,10,15-tetraamine (OTP-OMeDPA)

A dried three-neck round bottom flask was charged with 4Cl-OTP (442 mg, 1 mmol), 4,4′-dimethoxydiphenylamine (1123 mg, 5 mmol), $Pd_2(dba)_3$ (137 mg, 0.15 mmol), $P(t\text{-}Bu)_3{\cdot}HBF_4$ (87 mg, 0.30 mmol), NaO(*t*-Bu) (960 mg, 10 mmol), and toluene (50 mL). The reaction mixture was refluxed overnight under argon. After cooling, the mixture was filtered through a silica gel pad. The filtrate was concentrated in vacuum and purified by column chromatography (THF/petroleum ether 60–90 °C, 3/7, *v/v*) on silica gel to afford a beige solid as the desired product (1120 mg, 91% yield). ^1H NMR (500 MHz, THF-d_8) δ: 6.99–6.95 (m, 16H), 6.81–6.77 (m, 20H), 6.65 (dd, J_1 = 3.2 Hz, J_2 = 3.2 Hz, 4H), 6.57 (d, J = 3.1 Hz, 4H), 3.75 (s, 24H) ppm. ^{13}C NMR (125

MHz, THF-d_8) δ: 157.22, 148.52, 141.80, 134.74, 127.94, 120.34, 118.80, 115.99, 55.75 ppm. HR-MS (MALDI-TOF) *m/z* calcd. for $[M]^+$: 1212.5032. Found: 1212.5032.

1.4. Synthesis of 4,4',4'',4'''-(7,7',7'',7'''-(tetraphenylene-2,7,10,15-tetrayl)tetrakis(2,3-dihydrothieno[3,4-*b*][1,4]dioxine-7,5-diyl))tetrakis(*N*,*N*-bis(4-methoxyphenyl)aniline) (OTPE-OMeTPA)

A mixture of 4Cl-OTP (0.71 g, 1.60 mmol), 4-methoxy-*N*-(4-methoxyphenyl)-*N*-(4-(7-(tributylstannyl)-2,3-dihydrothieno[3,4-*b*][1,4]dioxin-5-yl)phenyl)aniline (7.06 g, 9.60 mmol), and $Pd(PPh_3)_4$ (184 mg, 0.16 mmol) in dry toluene (100mL) was refluxed for 24 h under argon. After cooling the reaction mixture, 100 mL of water was added and the mixture was extracted three times with chloroform (3×80 mL). The combined organic layers were washed with brine and water in turn. After removing solvent under reduced pressure, the residue was purified by column chromatography (THF/petroleum ether 60–90 °C, 1/1, *v*/*v*) on silica gel to afford a yellow solid as the desired product (2393 mg, 72% yield). ^{1}H NMR (400 MHz, THF-d_8) δ: 7.67 (dd, J_1 = 1.9 Hz, J_2 = 1.9 Hz 4H), 7.59 (d, J = 1.8 Hz, 4H), 7.54–7.51 (m, 8H), 7.17 (d, J = 8.1 Hz, 4H), 7.01–6.98 (m, 16H), 6.85–6.80 (m, 24H), 4.29 (br, 16H), 3.74 (m, 24H) ppm. ^{13}C NMR (100 MHz, THF-d_8) δ: 157.34, 148.47, 143.02, 141.85, 140.47, 140.45, 139.04, 133.69, 130.34, 127.57, 127.41, 127.22, 126.53, 125.79, 121.44, 116.66, 115.58, 114.08, 55.74 ppm. HR-MS (MALDI-TOF) *m/z* calcd. for $[M]^+$: 2077.60452. Found 2077.60354.

1.5. Hole mobility measurement

An indium-doped tin-oxide (ITO) coated glass substrate was patterned by laser etching. The substrate was carefully cleaned in ultrasonic baths of detergent, deionized water, ethanol, and acetone, alternately. A 40-nm-thick PEDOT:PSS layer was spin-coated at 3000 rpm for 30 s onto the ITO substrate, which was then annealed at 150 °C for 15 min in air. The chlorobenzene solution of OTP-OMeDPA (100 mM) or OTPE-OMeTPA (80 mM) was spin-coated at 5000 rpm for 30 s to yield a flat ~200-nm-thick thin film. For doped samples, BPTFSI and TBP were added to the solution at molar ratios of 0.5 and 2.8. A 120-nm-thick gold layer was then evaporated onto the active layer under high vacuum (<10^{-4} Pa). Dark *J*–*V* curves were measured with a Keithley 2400 Source-Measure unit. The hole mobility (μ_h)was determined by fitting *J*–*V* curves with the Mott-Gurney law[S4,S5]

$$J_h = \frac{9}{8}\varepsilon_0\varepsilon_r\mu_h\frac{V^2}{L^3}, \quad (1)$$

where J_h is the hole current density, V is the aplied voltage, ε_0 and ε_r are the vacuum and relative permittivities, respectively, and L is the thickness of hole transport layer.

1.6. Electrical conductivity measurement

Direct-current electrical conductivity (σ) of an organic thin film contacted with interdigitated gold electrodes was derived from current–voltage (*I*–*V*) curve in the bias range from −1.5 V to 1.5 V. The number (n) of channels in interdigitated electrodes on SiO_2 is 119, the channel length (L) is 1.5 mm, the channel width (W) is 10 μm, and the channel thickness (t) is 110 nm. The organic film was spin-coated from a chlorobenzene solution of OTP-OMeDPA (40 mM) or OTPE-OMeTPA (30 mM) at a spin speed of 2,000 rpm. For doped samples, BPTFSI and TBP were added to the solution at molar ratios of 0.5 and 2.8. The device was stored under dry air (< 5% RH) for 3 d before measurement. *I*–*V* curve was recorded on a CHI660C electrochemical workstation. Electrical conductivity was calculated by equation

$$\sigma = s\frac{W}{nLt}, \quad (2)$$

where s is the slope derived from the linear fitting of *I*–*V* plot.

1.7. Fabrication, encapsulation, and disassembly of perovskite solar cell

A laser etched fluorine doped tin oxide (FTO) glass (TEC 14, Nippon Sheet Glass Co., Ltd, white glass, 1.6 mm thickness, 25 mm × 16 mm) was rinsed in turn with detergent, deionized water, acetone, and ethanol for 10 min using an ultrasonic bath. Thereafter, a compact TiO_2 blocking layer was deposited onto the FTO glass at 450 °C via spray pyrolysis of an alcoholic solution of TIACA (40 mM) and ACAC (400 mM). Next, a mesoporous TiO_2 layer at the thickness of ~200 nm was coated by spin-coating of a TiO_2 colloidal solution at 4000 rpm for 10 s, with a ramp rate of 2000 rpm s^{-1}. The TiO_2 solution was prepared in advance by diluting the commercial 30NR-D TiO_2 paste with anhydrous ethanol at a weight ratio of 1:6. After solidification at 80 °C in air for 10 min, the mesoporous film was obtained via sintering at 450 °C with a flow of dry air for 30 min to wipe off all carbon components. The perovskite precursor solution was prepared by dissolving 1.30 M of PbI_2, 1.19 M of FAI, 0.14 M of $PbBr_2$, 0.14 M of MABr, and 0.07 M of CsI in the DMSO and DMF mixture (*v*:*v*, 1:4). The deposition of a triple cation

perovskite film was carried out with two-step spin-coating at 1000 rpm for 10 s (ramp rate 200 rpm s^{-1}) and 6000 rpm for 30 s (ramp rate 2000 rpm s^{-1}). Note that 150 μL of CB was dripped on the substrate at the time of 15 s before the spin end. The deposited film was subsequently annealed at 120 °C for 1 h to produce the black perovskite. A hole transport layer with a thickness of ~90 nm was spin-coated atop the annealed perovskite film from a chlorobenzene solution of spiro-OMeTAD (40 mM), OTP-OMeDPA (40 mM), or OTPE-OMeTPA (30 mM) at 4000 rpm for 20 s for the standard devices if there is no specific statement. The layers were doped with BPTFSI and TBP at molar ratios of 0.5 and 2.8. The depositions of perovskite layer and hole-transporting layer were carried out in a dry air-filled glove box with a < 2% relative humidity. Finally, a ~120 nm-thick, gold electrode was deposited by thermal evaporation under a ≤ 1×10^{-4} Pa vacuum to complete the cell fabrication. The device stored under dry air (< 5% RH) overnight was laminated with a waterproof adhesive tape and further encapsulated by an epoxy adhesive (3M) hermetically. This cell is referred as "fresh cell" in the main text. The cell active area is ~0.5 × 0.5 cm^2. If it was necessary, encapsulation materials and gold layers were torn off by a knife before measurements.

1.8. Aging at 60 °C

The encapsulated cell was stored at 60 °C in a FD56 oven (Binder, Germany) for long-term thermal stability evaluation with an environmental relative humidity of 45–85%. The cell was taken out from oven at a regular-interval for measurement. The 60 °C 1000 h aged cell is referred as "aged cell" in the main text. If it was necessary, encapsulation materials and gold layers were also torn off before measurements.

1.9. Current density–voltage curve, external quantum efficiency, and impedance measurements

Current density–voltage characteristics were recorded by applying a bias potential to a testing cell and measuring photocurrent with a Keithley 2400 source meter under the full computer control. The measurements were fully automated by using Labview 14.0. A Sirius-SS150A solar simulator (Zolix, China) was used to give an irradiance of 100 mW cm^{-2}. The light intensity was tested with a calibrated monocrystalline silicon solar cell (Model HG-SS20, No. L0013, Beijing Henggong Instrument Co. Ltd., China). A metal mask with an aperture area of 0.16 cm^2 was covered on a testing cell during all measurements in a nitrogen-filled glovebox. An Omni-λ300 monochromator (Zolix, China) collocated with a 150 W xenon lamp (Zolix, China) was employed to supply monochromatic lights for EQE measurements, at a 10 nm wavelength interval. A Keithley 2400 source meter under the full computer control with Labview 14.0 was deployed to short-circuit a solar cell and meanwhile measure the currents at a current sampling time of 1 s. A Hamamatsu S1337-1010BQ silicon diode calibrated at the National Institute of Metrology, China was used to measure the intensities of monochromatic lights. Impedance spectra of fresh and aged PSCs at a forward bias in the dark were recorded on an AutolabPGSTAT302N electrochemical workstation by applying a 40 mV voltage perturbation, with the frequency range from 1 MHz to 100 Hz. The measured impedance spectra were fitted using the Z-view software (v2.80, Scribner Associates Inc.).

2. Theoretical modeling

2.1. Molecule geometry, frontier molecular orbital, and energy level

Density functional theory (DFT) and time dependent DFT (TDDFT) calculations of OTP-OMeDPA and OTPE-OMeTPA were carried out with the Gaussian 09 program suite, using the 6-311G(d,p) basis set for all atoms. The integral equation formalism polarizable continuum model (IEFPCM) was chosen for the solvent (THF) effect modeling.[S6] Optimization of ground-state geometries was carried out by using the popular B3LYP exchange-correlation functional.[S7] The PBE1PBE[S8] and BMK[S9] hybrid functionals were used to calculate 40 vertical electron transitions and excited-state properties.

2.2. Hole extraction by hole transport layer from photoexcited perovskite

The rate constant of hole extraction by hole transport layer (*j*) from photoexcited perovskite (*i*), ω_{ij}, can be described by the Marcus electron transfer theory[S10] via equation

$$\omega_{ij} = \frac{2\pi}{\mathrm{h}} \frac{v_{ij}^{\ 2}}{\sqrt{4\pi\lambda_{\mathrm{he}} k_{\mathrm{B}} T}} \exp\left[-\frac{\left(\Delta G_0 - \lambda_{\mathrm{he}}\right)^2}{4\lambda_{\mathrm{he}} k_{\mathrm{B}} T} \right], \tag{3}$$

where h is the reduced Planck constant, T the Kelvin temperature, k_{B} the Boltzmann constant, v_{ij} the transfer integral between perovskite and hole transport layer, ΔG_0 the driving force of hole extraction, and λ_{he} the reorganization energy of hole extraction. λ_{he} is composed of the internal reorganization energy (λ_{int}) and the external reorganization energy (λ_{out}). λ_{out} can be ignored because of its little contribution in solid state. The contribution to λ_{int} from photoexcited perovskite can also be neglected. Thus λ_{he} of hole extraction can be approximately calculated by

$$\lambda_{he} \approx E_{+}^{*} - E_{+},$$

(4)

where E_{+}^{*} and E_{+} represent the energies of ion in neutral geometry and ion in ion geometry for the hole transport molecule. The λ_{he} value was calculated using DFT at the B3LYP/6-311G(d,p) level.

2.3. Kinetic Monte Carlo (kMC) simulation of hole transport

In general, the hole transport process in an organic solid can be well described by the hopping model where a hole is assumed to instantaneously localize on one molecule, i.e. a hopping site. The rate constant of hole transfer (ω_{ij}) can also be described by the Marcus theory as

$$\omega_{ij} = \frac{2\pi}{\mathrm{h}} \frac{v_{ij}^{2}}{\sqrt{4\pi\lambda_{ht} k_{B} T}} \exp\left[-\frac{\left(\Delta E_{ij} - \lambda_{ht}\right)^{2}}{4\lambda_{ht} k_{B} T} \right], \tag{5}$$

where v_{ij} is the transfer integral between the *i* and *j* hopping sites, ΔE_{ij} is the site energy difference of the *i* and *j* hopping sites, and λ_{ht} is the reorganization energy of hole transport. v_{ij} indicates the strength of electronic coupling between the highest occupied molecular orbitals (HOMO) of two adjacent molecules. ΔE_{ij} is mainly contributed by electrostatic interactions and polarization effects from environment,[S11] which bring forth the HOMO variation of an isolated molecule. λ_{int} is dependent of the change of molecular geometries accompanied by the progress of hole transfer. From four energies of adiabatic potential-surface (AP), λ_{ht} can be calculated by

$$\lambda_{ht} \approx \lambda_{int} = \lambda_{0}^{AP} + \lambda_{+}^{AP} = E_{0}^{*} - E_{0} + E_{+}^{*} - E_{+}, \tag{6}$$

where λ_{0}^{AP} and λ_{+}^{AP} are the reorganization energy for neutral geometry and cationic geometry respectively. E_{0}^{*} and E_{0} represent the energies of neutral in ion geometry and neutral in neutral geometry, E_{+}^{*} and E_{+} represent the energies of ion in neutral geometry and ion in ion geometry. The λ_{ht} value was calculated using DFT at the B3LYP/6-311G(d,p) level.

On the basis of the amorphous structure at 300 K afforded by molecular dynamics (MD) simulation, hole transport dynamics was investigated. Firstly, the neighbor list, including all molecule pairs, was established for two adjacent molecules with a nearest atom-to-atom distance no larger than 5 Å. The electrostatic and polarization contributions were calculated based on the Thole model,[S11] and the partial charges of neutral and cationic states needed in this model were generated by DFT calculations at the CAM-B3LYP/6-311G(d,p) level. In addition, the Gaussian disorder model was applied to extract the energetic disorder by fitting the ΔE_{ij} distribution. To effectively calculate v_{ij} of every molecular pair *ij* in the neighbor list, an approximate method based on the Zerner's independent neglect of differential overlap (ZINDO) was employed.[S12] The results obtained from the time-saving ZINDO method have been demonstrated to be reasonably consistent with those computed at the B3LYP/6-31G(d) level.[S13]

After determining the hopping sites and the hole transfer rates for each hopping site, the next task is to solve the master equation which describes the time evolution of a hole in the amorphous system,

$$\frac{\partial p_{i}}{\partial t} = \sum_{j} p_{j} \omega_{ji} - \sum_{j} p_{i} \omega_{ij}, \tag{7}$$

Where p_{i} and p_{j} are the occupation probability of a hole in the *i* and *j* hopping sites. The solution of the master equation can be obtained by using kinetic Monte Carlo (kMC) methods, which explicitly simulates the dynamics of hole by constructing a Markov chain in state space.

Therefore, after all parameters defined for each hopping site were computed, stochastic kMC simulations[S14] were performed with a simulation time of 10 μs for an ordered structure and 1 ms for a disordered structure. Theoretical μ_{h} was determined from the time-evolution of kMC trajectories. The diffusion coefficient (D) of a hole was obtained from a linear fit to the mean square displacement (MSD) according to

$$D = \frac{1}{2n} \frac{\mathrm{dMSD}^{2}}{\mathrm{d}t}, \tag{8}$$

where n is the dimensionality of the amorphous cell and t is the simulation time. In the end, μ_{h} was derived via the Einstein-

Smoluchowski relation

$$\mu_{\mathrm{h}} = \frac{eD}{k_B T}, \tag{9}$$

where e is the elementary charge.

2.4. Modeling glass transition temperature of organic amorphous solid

By use of the amorphous cell module in Materials Studio package,[S15] four unit cells with periodic boundary for the OTP-OMeDPA solid (480 molecules), the OTPE-OMeTPA solid (480 molecules), the OTP-OMeDPA/BPTFSI composite (480 OTP-OMeDPA molecules and 240 BPTFSI molecules), and the OTPE-OMeTPA/BPTFSI composite (480 OTPE-OMeTPA molecules and 240 BPTFSI molecules) were constructed. The force field of condensed-phase optimized molecular potential for atomistic simulation studies II (COMPASS II)[S16] was utilized in the MD simulations. In the COMPASS II force field, the potential energy (E_{pot}) is described by

$$E_{\mathrm{pot}} = E_{\mathrm{bond}} + E_{\mathrm{cross}} + E_{\mathrm{non}}, \tag{10}$$

where E_{bond} , E_{cross} , and E_{non} are the bonded energy, the cross energy, and the nonbonded energy, respectively. MD simulations started from 700 K under the canonical ensemble for 1 ns total simulation time with 1 fs time step by a Nose thermostat. Next, the production was carried out for another 1 ns under isothermal-isobaric ensemble by keeping the pressure at 1 atm. The temperature was decreased to 250 K at 20 K interval during the simulations with the FORCITE module in the Materials Studio package. We derived the $T_{\mathrm{g}}^{\mathrm{sp}}$ value from the crossing point of linear fittings of specific volume at high and low temperatures.

2.5. Diffusion of CH_3I in organic amorphous solid

In order to model the physical diffusion of iodine species in an amorphous organic film, which can be released due to the thermal decomposition of organic-inorganic hybrid perovskite, we insert 40 extra CH_3I molecules into the above constructed boxes. Heating and cooling cycle processes were followed in the isothermal-isobaric ensemble, within the temperature range from 300 to 700 K at 25 K interval. Next, MD simulations in the isothermal-isobaric ensemble (333 K, 1 bar) were performed for 1 ns. At the end, MD simulation in the canonical ensemble (333 K) was performed for 1 ns to track the diffusion trajectories of CH_3I. D of CH_3I can be estimated by

$$D = \frac{1}{6N} \lim_{t \to \infty} \frac{\mathrm{d}}{\mathrm{d}t} \left\langle \sum_{i}^{N} [r_i(t) - r_i(0)]^2 \right\rangle, \tag{11}$$

where N is the number of gas molecules while $r_i(t)$ and $r_i(0)$ refer to the final and initial positions of the mass centers of gaseous CH_3I molecules over the time interval (t), respectively. The term of $\sum_{i}^{N} [r_i(t) - r_i(0)]^2$ means the ensemble average of mean square displacement of CH_3I.

3. Additional data

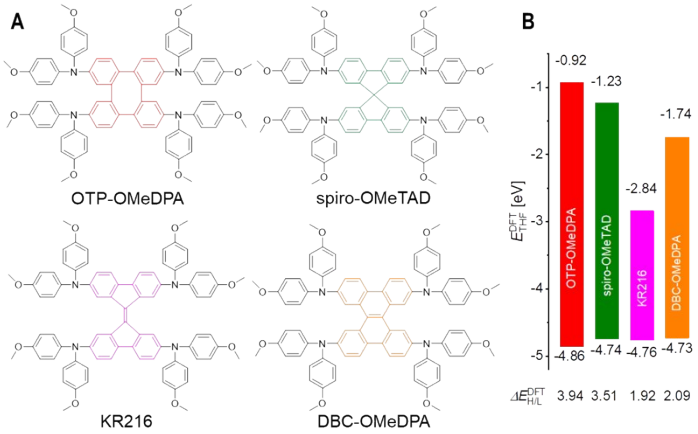

Fig. S1 (A) Four structurally related arylamines: OTP-OMeDPA, spiro-OMeTAD[S17], KR216[S18], and DBC-OMeDPA[S19]. (B) Theoretical energy levels (E^{DFT}_{THF}) of LUMO (values above color bars) and HOMO (value under color bars) of molecules in THF. The HOMO/LUMO energy gaps ($\Delta E^{DFT}_{H/L}$) are also given.

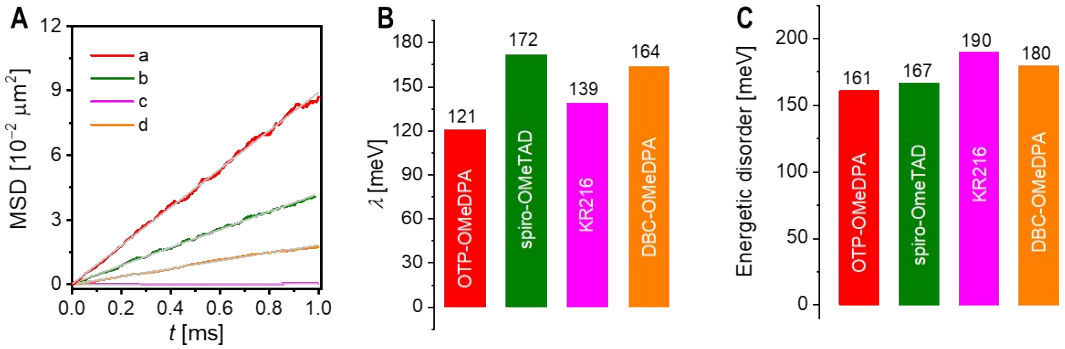

Fig. S2 (A) Mean square displacement (MSD) of a hole as a function of time (t) in the organic amorphous solids: (a) OTP-OMeDPA, (b) spiro-OMeTAD, (c) KR216, and (d) DBC-OMeDPA. The theoretical hole mobility (μ_h) is calculated by equation $\mu_h = \frac{e}{2nk_BT}\frac{\mathrm{dMSD}}{\mathrm{d}t}$, where e is elementary charge, n is transport dimension, k_B is Boltzmann constant, and T is Kelvin temperature. The μ_h values are 5.7×10^{-6} cm^2 V^{-1} s^{-1} for OTP-OMeDPA, 2.7×10^{-6} cm^2 V^{-1} s^{-1} for spiro-OMeTAD, 2.3×10^{-8} cm^2 V^{-1} s^{-1} for KR216, and 1.2×10^{-6} cm^2 V^{-1} s^{-1} for DBC-OMeDPA. (B) Reorganization energy (λ) of hole transport calculated by the adiabatic potential-surface method. (C) Energetic disorder derived from a Gaussian fitting of distribution of site energy difference.

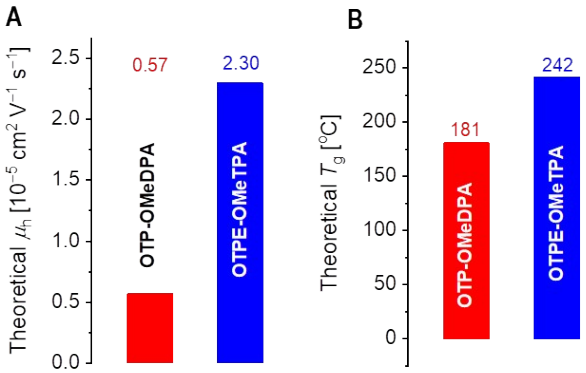

Fig. S3 (A) The theoretical hole mobility (μ_h) in the amorphous solids. (B) Theoretical glass transition temperature (T_g^{sp}) derived from temperature (T) dependent specific volume (V_{sp}).

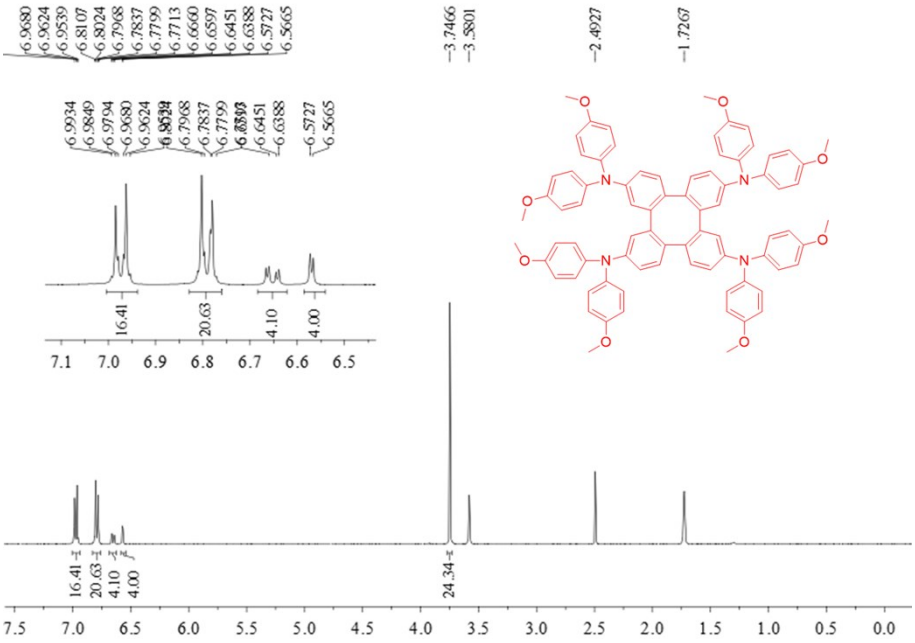

Fig. S4 The ^{1}H NMR (400 MHz) spectrum of OTP-OMeDPA in THF-d_8.

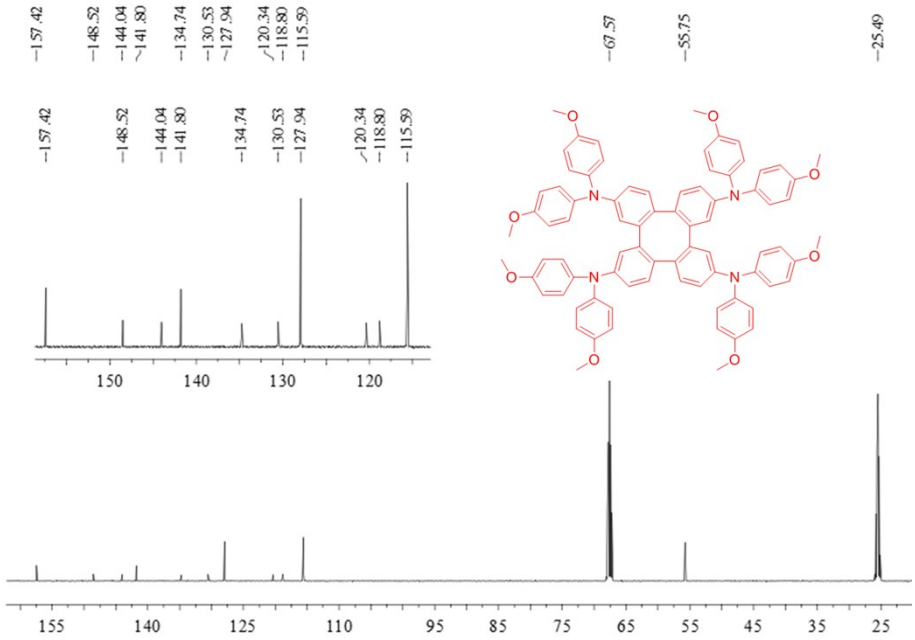

Fig. S5 The ^{13}C NMR (100 MHz) spectrum of OTP-OMeDPA in THF-d_8.

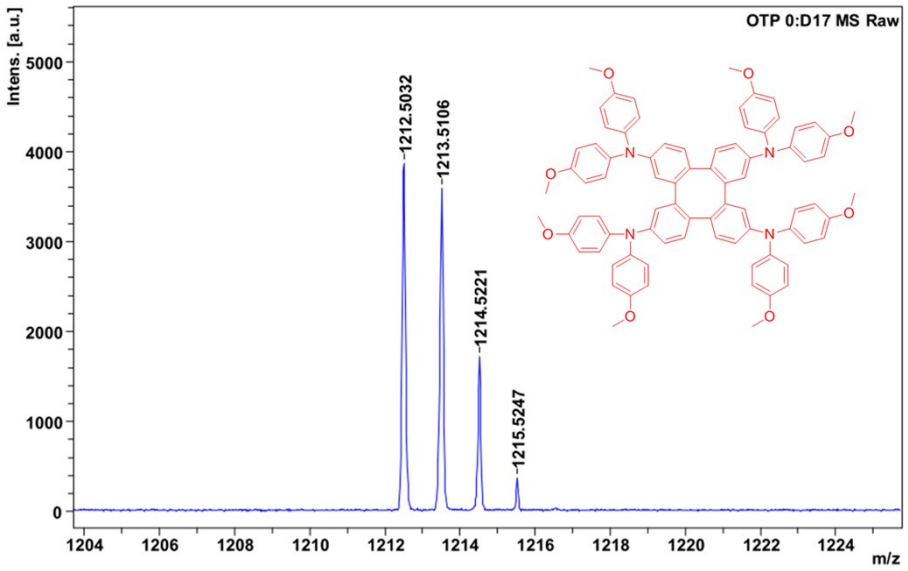

Fig. S6 The MALDI-TOF mass spectrum of OTP-OMeDPA.

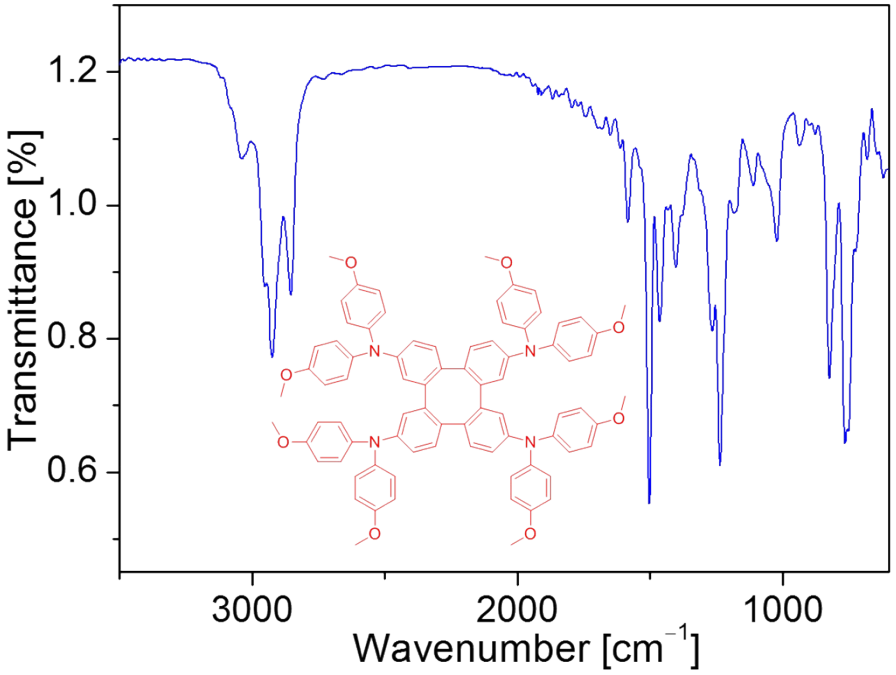

Fig. S7 The infrared spectrum of OTP-OMeDPA.

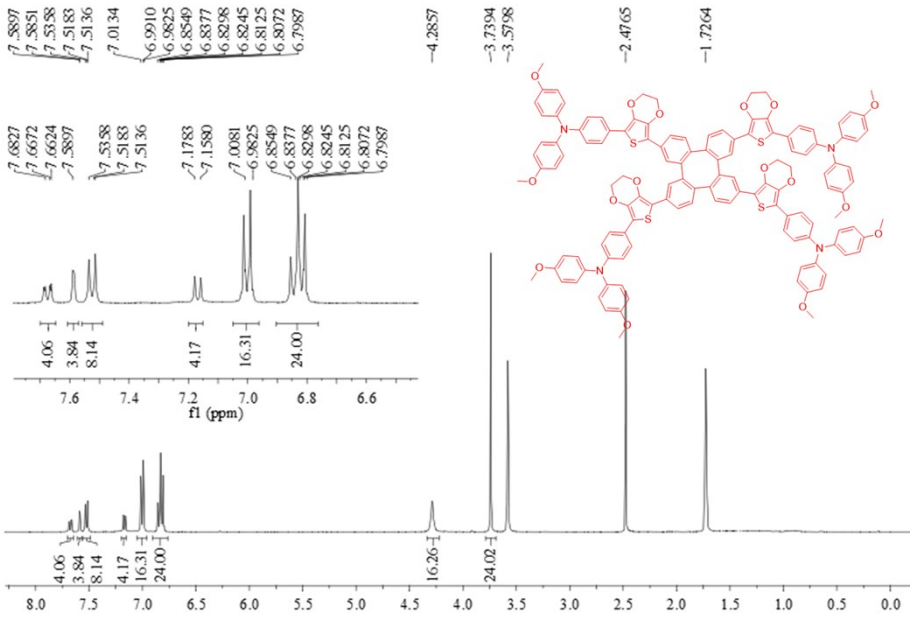

Fig. S8 The ^{1}H NMR (400 MHz) spectrum of OTPE-OMeTPA in THF-d_8.

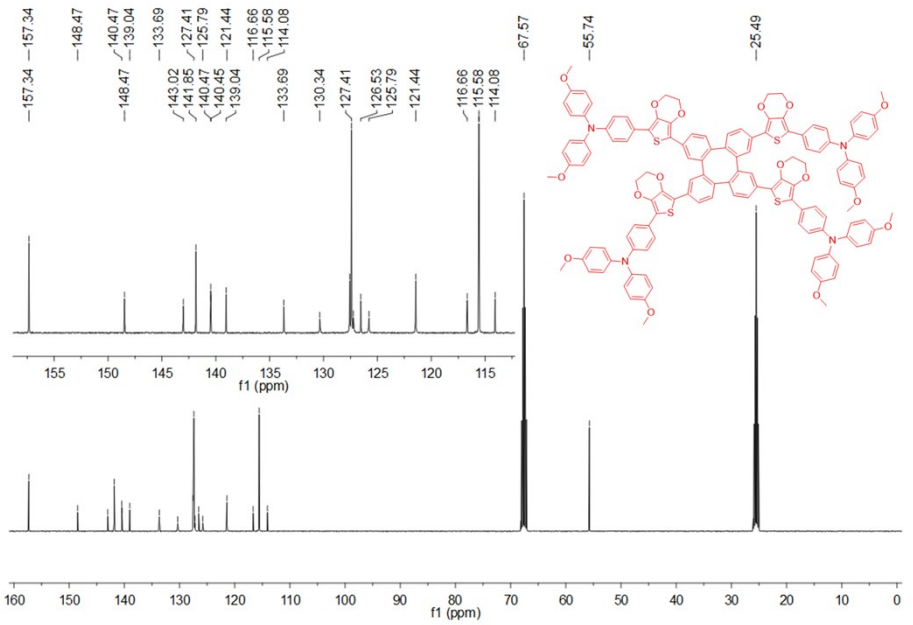

Fig. S9 The ^{13}C NMR (100 MHz) spectrum of OTPE-OMeTPA in THF-d_8.

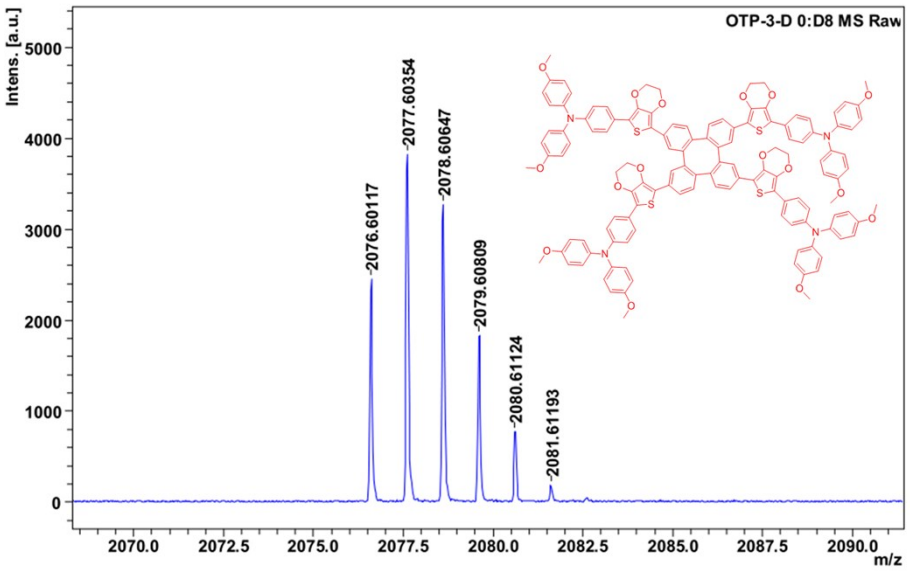

Fig. S10 The MALDI-TOF mass spectrum of OTPE-OMeTPA.

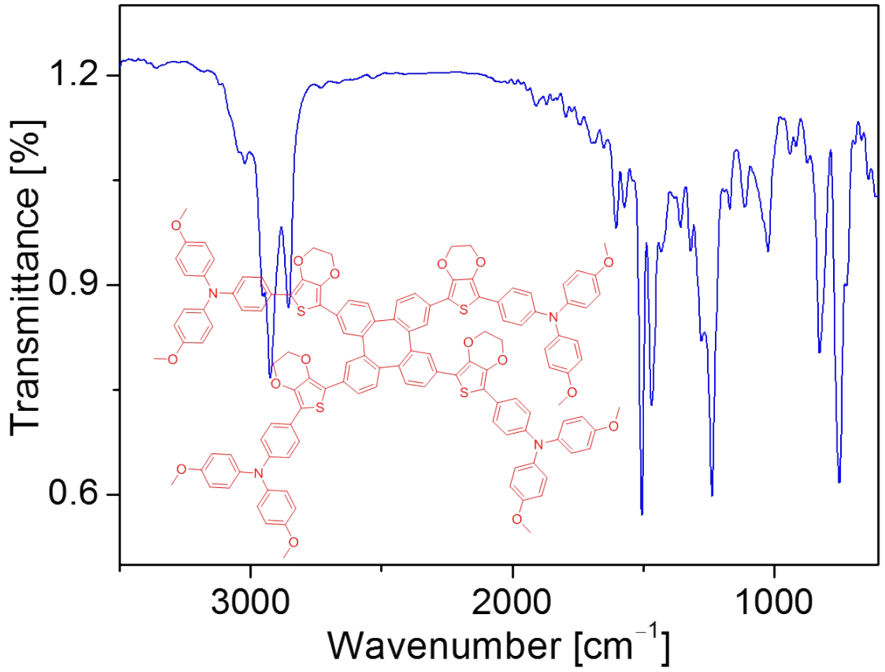

Fig. S11 The infrared spectrum of OTPE-OMeTPA.

Table S1 Crystal data and structure refinement of OTP-OMeDPA

Compound	OTP-OMeDPA
Empirical formula	$C_{80}H_{68}N_4O_8$
Formula weight	1213.39
Temperature	170 K
Wavelength [Å]	0.71073
Crystal system	Triclinic
Space group	$P\bar{1}$
a [Å]	13.1843 (4)
b [Å]	15.6772 (4)
c [Å]	16.7764 (5)
α [°]	105.137 (1)
β [°]	94.300 (1)
γ [°]	105.266 (1)
Volume [Å^3]	3190.45 (16)
Z [Å^3]	2
ρ_{calc}[g cm^{-3}]	1.263
μ [mm^{-1}]	0.082
F [000]	1280.0
Crystal size [mm^3]	0.26×0.09×0.07
2Θ range for data collection [°]	2.30 to 27.05
Refl. Collected	54199
Independent reflections	14065
Data/restraints/parameters	14065/0/837
Data completeness	0.999
Goodness-of-fit on F^2	1.052
Final *R* indexes [*I*>=2σ (*I*)]	R1 = 0.0458, wR2 = 0.1054
Final *R* indexes [all data]	R1 = 0.0582, wR2 = 0.1145
Largest diff. peak/hole [e Å^{-3}]	0.276/–0.309
CCDC deposition number	2052553

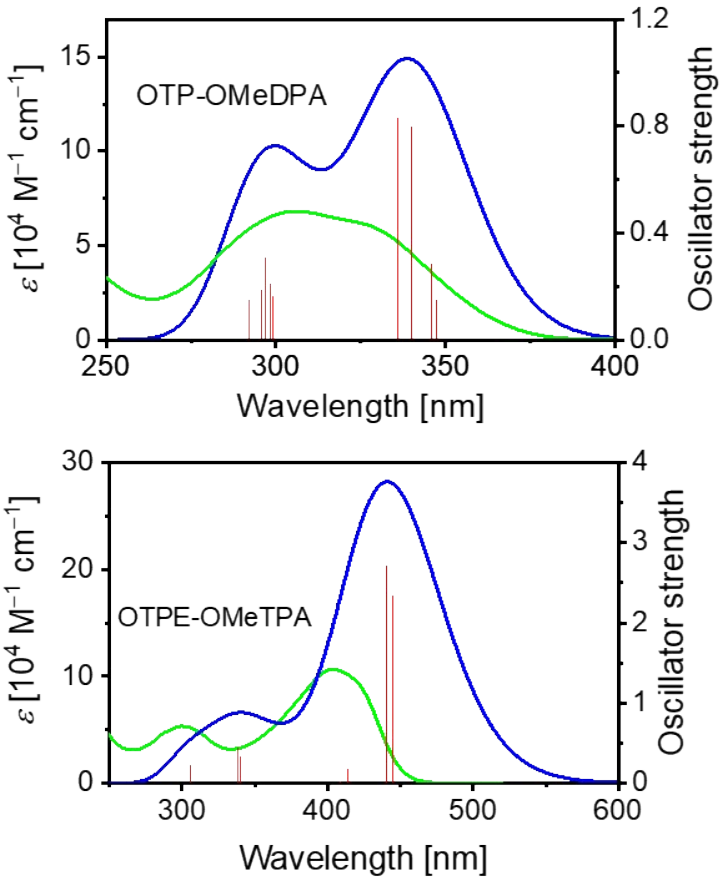

Fig. S12 Theoretical electronic absorption spectra (blue) based on TDDFT calculations at the PBE1PBE/6-311G(d,p) level for each molecule in THF. Vertical excitation energies are shown by vertical lines (red) according to oscillator strengths. Experimental spectra (green) are also included.

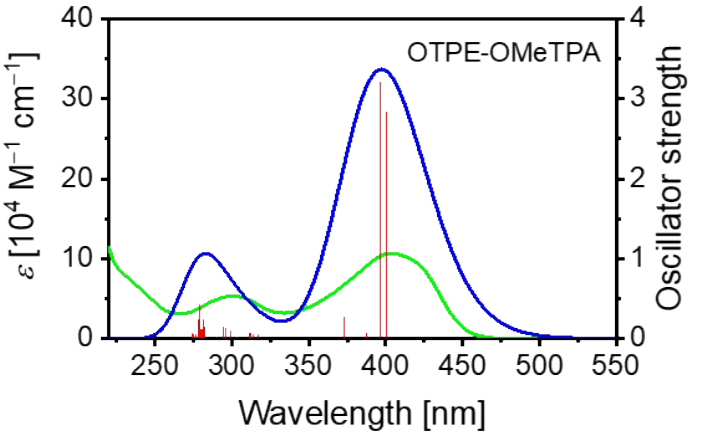

Fig. S13 Theoretical electronic absorption spectrum (blue) based on TDDFT calculation at the BMK/6-311G(d,p) level for molecule in THF. Vertical excitation energies are shown by vertical lines (red) according to oscillator strengths. Experimental spectrum (green) is also included.

Table S2 Theoretical excitation energy, oscillator strength, and transition assignment of OTP-OMeDPA[a]

Excitation energy [nm]	Oscillator strength	Transition	Related orbital
347	0.15	$S_0 \rightarrow S_1$	H → L (25%) H → L+1 (24%) H → L+2 (13%)
346	0.29	$S_0 \rightarrow S_2$	H → L (45%) H → L+1 (21%)
340	0.80	$S_0 \rightarrow S_5$	H–1 → L+3 (17%) H → L+3 (45%) H → L+4 (15%)
336	0.83	$S_0 \rightarrow S_6$	H–1 → L+3 (25%) H–1 → L+4 (22%) H → L+3 (17%) H → L+4 (14%)

[a]H and L refer to HOMO and LUMO, respectively. Typical electron transitions of the low-energy band are given. Excitation energy, oscillator strength, and transition assignment are obtained from TDDFT calculation at the PBE1PBE/6-311G(d,p) level in THF.

Table S3 Theoretical excitation energy, oscillator strength, and transition assignment of OTPE-OMeTPA[a]

Excitation energy [nm]	Oscillator strength	Transition	Related orbital
400	2.84	S0→S1	H–3 → L+2 (13%) H–1 → L (21%) H → L (33%)
396	3.20	S0→S2	H–2 → L+3 (14%) H–1 → L+1 (24%) H → L+1 (27%)

[a]H and L refer to HOMO and LUMO, respectively. Typical electron transitions of the low-energy band are given. Excitation energy, oscillator strength, and transition assignment are obtained from TDDFT calculations at the BMK/6-311G(d,p) level in THF.

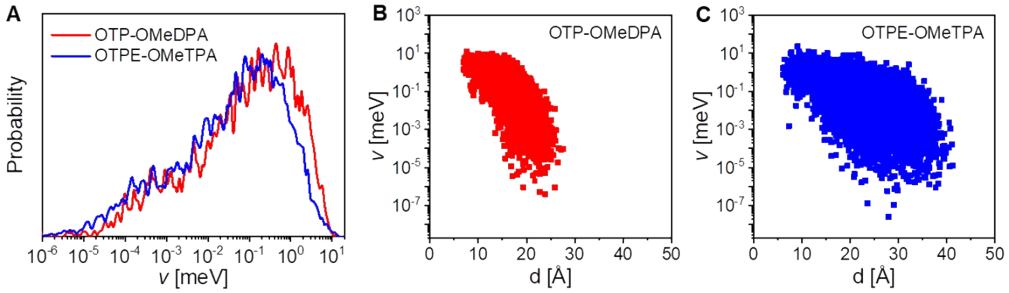

Fig. S14 (A) Distributions of transfer integrals (v) of the MD-simulated amorphous organic solids. (B, C) Plots of v as a function of centroid distance (d) for the OTP-OMeDPA system and the OTPE-OMeTPA system.

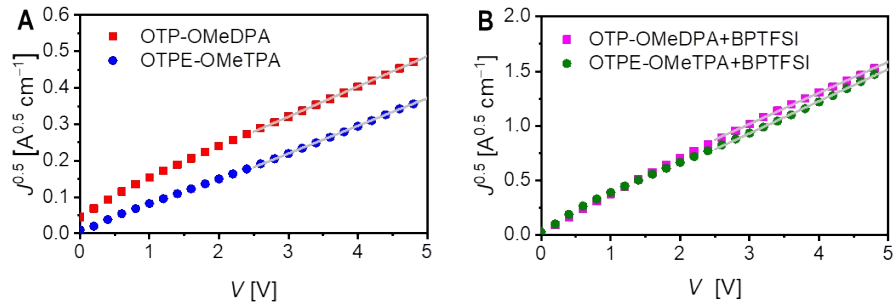

Fig. S15 Typical *J*–*V* curves of the hole-only devices with a configuration of ITO/PEDOT:PSS/HTL/Au. The data points are experimentally measured, and the gray lines in the range of 2.5–5 V are the fittings by equation $J = \frac{9}{8}\varepsilon_0\varepsilon_r\mu_h\frac{V^2}{d^3}$, where ε_0 is the vacuum permittivity, ε_r is the relative permittivity, μ_h is the mobility, and d is the film thickness.

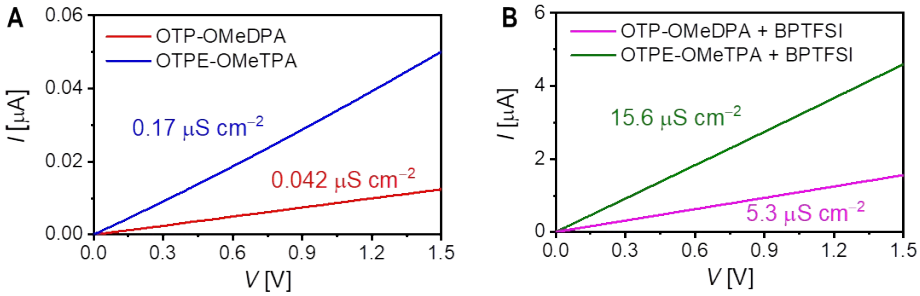

Fig. S16 *I*–*V* curves of thin films of (A) the pristine organic semiconductors and (B) the counterparts mixed with 0.5 equivalent BPTFSI deposited on interdigital electrodes. The direct current electrical conductivities are also included.

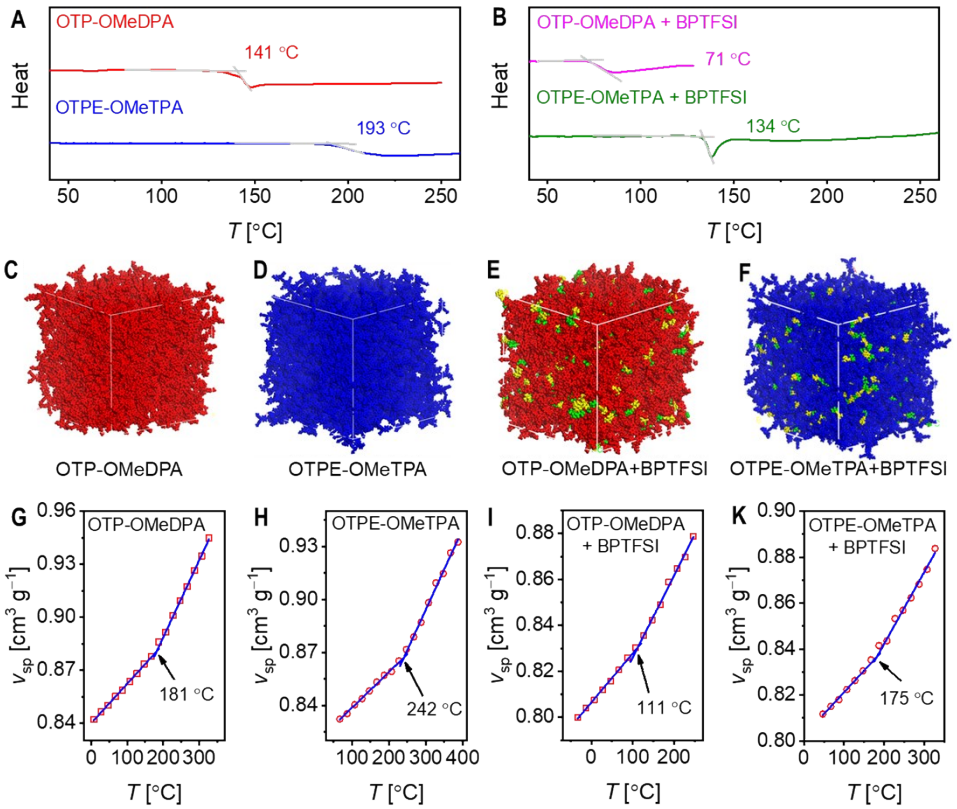

Fig. S17 Differential scanning calorimetry (DSC) thermograms of (A) pristine and (B) doped organic solid samples. (C–F) Representative snapshots of MD simulated amorphous systems with 480 organic semiconductor molecules, and composite systems with 360 organic semiconductor molecules and 240 BPTFSI molecules at 300K. OTP-OMeDPA molecules are colored by red, OTPE-OMeTPA molecules are colored by blue, BP cations are colored by yellow, TFSI anions are colored by green. In these four amorphous systems, molecules are randomly oriented and uniformly mixed. (G–K) Plots of simulated specific volume (V_{sp}) as a function of temperature (T) for pristine and doped organic amorphous solids.

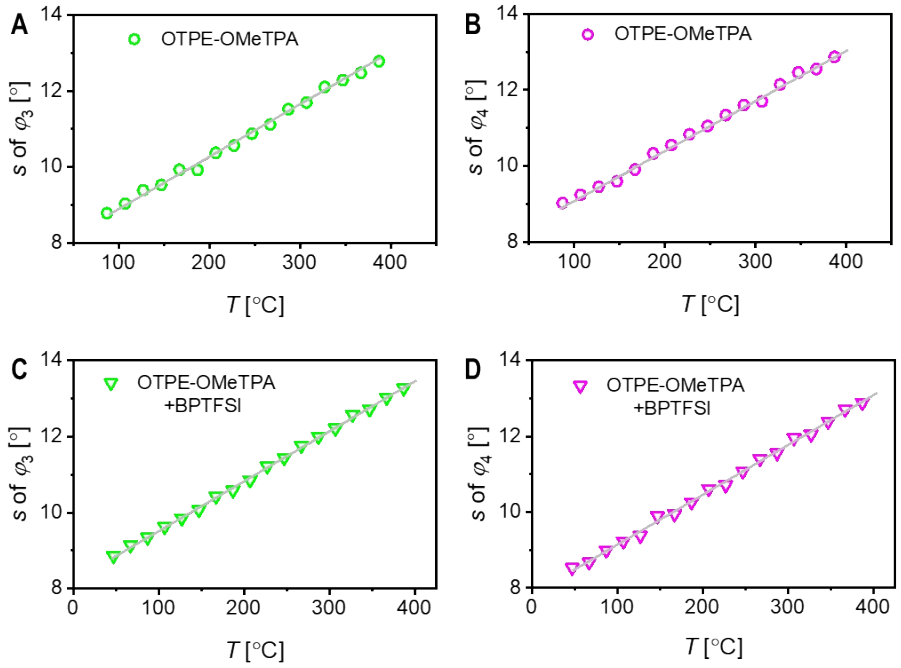

Fig. S18 Mean standard deviation (s) of φ_3 and φ_4 as a function of T in the pristine organic amorphous solids (A, B) and the analogues mixed with 0.5 equivalent BPTFSI (C, D). The gray lines are the linear fittings.

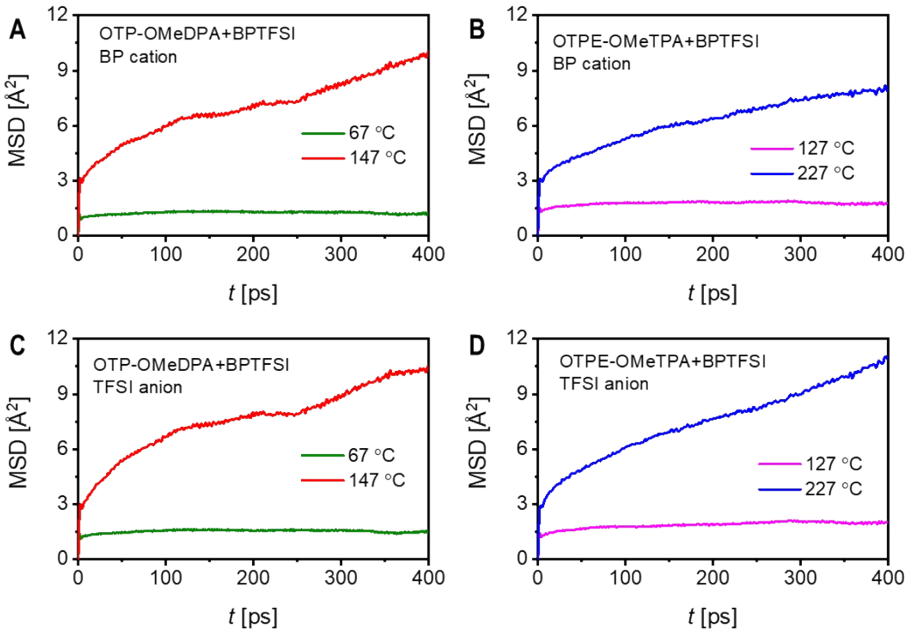

Fig. S19 Evolution of simulated MSD of BP cations and TFSI anions in the semiconducting composites at temperatures of ca. 40 °C above and below T_g^{sp}.

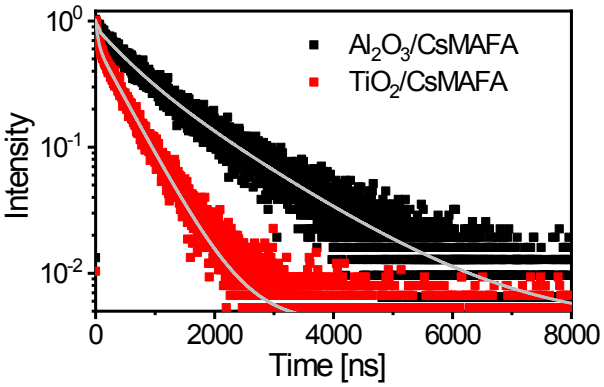

Fig. S20 TRPL trace of CsMAFA based perovskite film on mesoporous alumina or titania substrate.

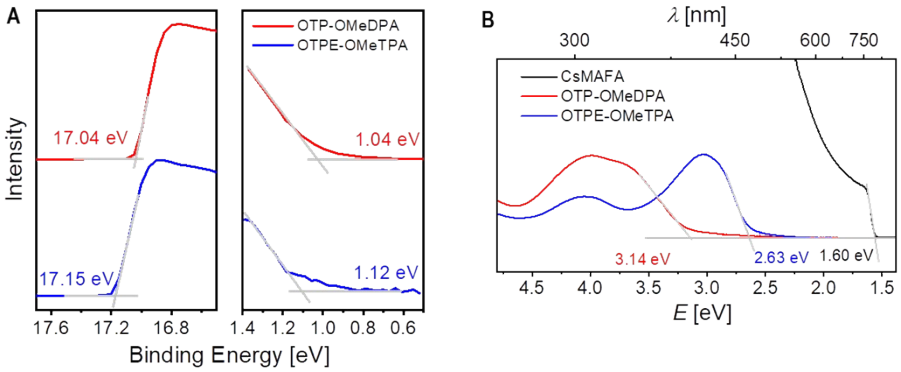

Fig. S21 (A) UPS spectra of spin-coated thin films on FTO glass with the cutoff (left) and onset (right) energy regions. The HOMO energy levels ($E_{\mathrm{H}}^{\mathrm{UPS}}$) can be deduced via equation $E_{\mathrm{H}}^{\mathrm{UPS}} = 21.1 - (E_{\mathrm{cutoff}} - E_{\mathrm{i}})$, being –5.00 eV for OTP-OMeDPA and –4.96 eV for OTPE-OMeTPA, where E_{i} and E_{cutoff} denote the onset and cutoff of binding energy, respectively. (B) Electronic absorption spectra of the herein used perovskite, OTP-OMeDPA and OTPE-OMeTPA. The perovskite film is spin-coated on the mesoporous titania substrate. OTP-OMeDPA and OTPE-OMeTPA are spun from chlorobenzene onto glass.

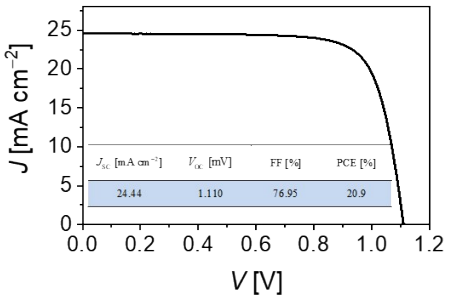

Fig. S22 *J*–*V* curve measured under the 100 mW cm^{-2}, AM1.5G sunlight for a typical PSC with spiro-OMeTAD.

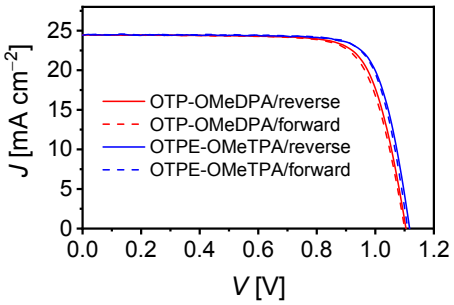

Fig. S23 *J*–*V* curves of forward and reverse scans for PSCs with OTP-OMeDPA or OTPE-OMeTPA as HTL under the 100 mW cm^{-2}, AM1.5G sunlight.

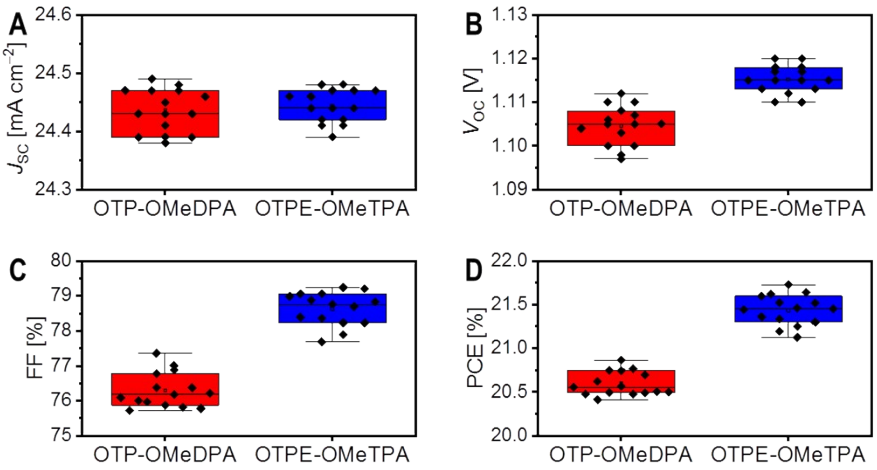

Fig. S24 Box plots of photovoltaic parameters of 16 cells.

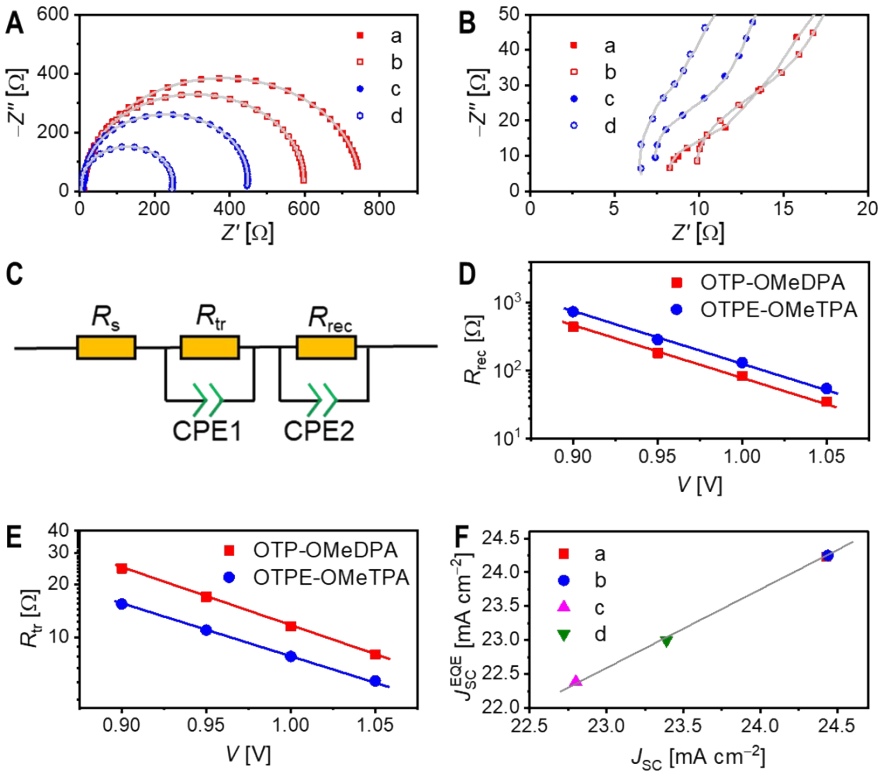

Fig. S25 (A) The Nyquist plots of PSCs and (B) the corresponding high-frequency regions measured at the forward bias of 0.90 V in the dark: (a) fresh cell with OTP-OMeDPA, (b) fresh cell with OTPE-OMeTPA, (c) aged cell with OTP-OMeDPA, and (d) aged cell with OTPE-OMeTPA. (C) The equivalent circuit used to fit impedance spectra of PSCs. (D) Plots of charge recombination resistance (R_{rec}) as a function of bias potential (V) for fresh PSCs. The lines are drawn as a guide to the eyes. (E) Plots of hole transport resistance (R_{tr}) versus V for fresh PSCs. The lines are drawn as a guide to the eyes. (F) Correlation between J_{SC}^{EQE} and J_{SC} for (a) fresh PSC with OTP-OMeDPA, (b) fresh PSC with OTPE-OMeTPA, (c) aged PSC with OTP-OMeDPA, and (d) aged PSC with OTPE-OMeTPA. The gray line is the linear fitting.

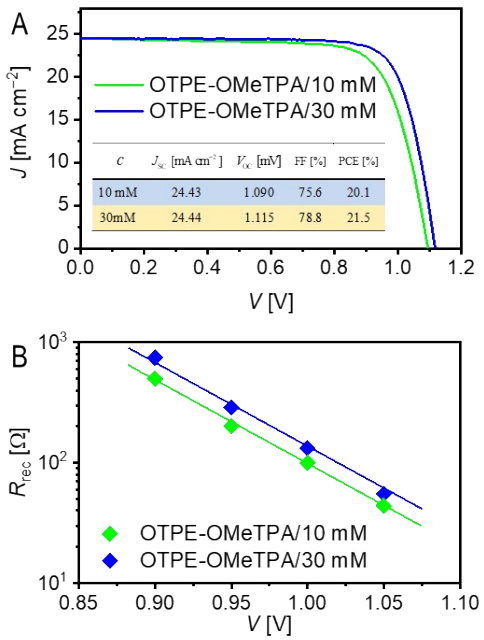

Fig. S26 (A) *J*–*V* curves measured under the 100 mW cm^{-2}, AM1.5G sunlight. (B) Plots of charge recombination resistance (R_{rec}) as a function of bias potential (V). The cells were fabricated from 10 mM and 30mM of OTPE-OMeTPA in chlorobenzene.

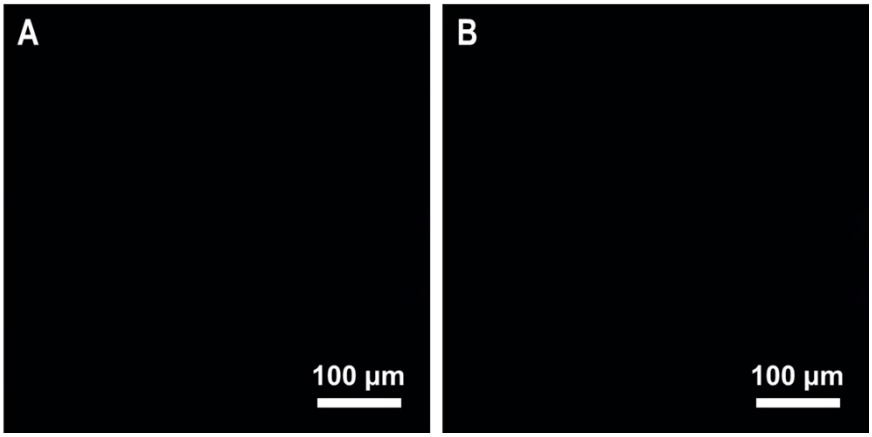

Fig. S27 Transmission polarization optical microscope images of fresh cells. The encapsulation materials and gold electrodes of PSCs were torn off before measurements.

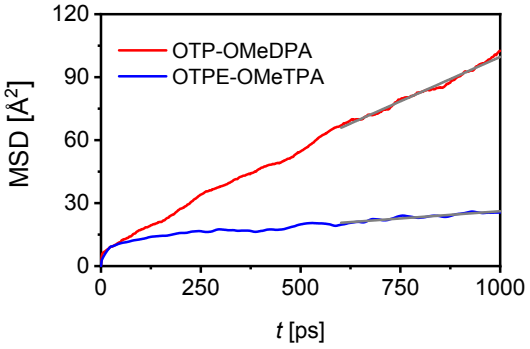

Fig. S28 Evolution of simulated MSD of CH_3I in the BPTFSI containing composite systems at 60 °C. The gray lines are the linear fittings to determine the diffusion coefficient of CH_3I.

Table S4 The time constants and corresponding amplitudes derived from TRPL decays of fresh and aged samples as well as charge separation yields[a]

Sample	Status	τ_1 [ns]	A_1	τ_2 [ns]	A_2	$\bar{\tau}$ [ns]	ϕ_c [%]
Al_2O_3/pvsk/PS	fresh	437.2	0.08	1511.9	0.92	1425.9	/
	aged	62.6	0.36	1307.7	0.64	865.4	/
TiO_2/pvsk/OTP-OMeDPA	fresh	18.8	0.89	98.2	0.11	27.3	98.1
	aged	32.3	0.76	293.3	0.24	94.9	89.0
TiO_2/pvsk/OTPE-OMeTPA	fresh	16.2	0.91	94.5	0.09	25.1	98.2
	aged	12.9	0.86	127.3	0.14	28.9	94.7

[a]The pvsk is the abbreviation of perovskite. τ_1 and τ_2 are the time constants of TRPL decay, A_1 and A_2 are the corresponding normalized amplitudes, and $\bar{\tau}$ is the amplitude average time constant calculated by equation $\bar{\tau} = A_1\tau_1 + A_2\tau_2$. ϕ_c is the yield of charge separation calculated by equation $\phi_c = 1 - \frac{\bar{\tau}_{TiO_2/pvsk/HTL}}{\bar{\tau}_{Al_2O_3/pvsk/PS}}$, where $\bar{\tau}_{Al_2O_3/pvsk/PS}$ is the amplitude average time constant of the perovskite film covered with a PS layer on alumina and $\bar{\tau}_{TiO_2/pvsk/HTL}$ is the amplitude average time constant of the perovskite film covered with a HTL on titania.

4. References

[S1] H. Jiang, Y. Zhang, D. Chen, B. Zhou and Y. Zhang, *Org. Lett.*, 2016, **18**, 2032.

[S2] Q. Feng, X. Jia, G. Zhou and Z. Wang, *Chem. Commun.*, 2013, **49**, 7445.

[S3] Y. Ren, M. Ren, X. Xie, J. Wang, Y. Cai, Y. Yuan, J. Zhang and P. Wang, *Nano Energy*, 2021, **81**, 105655.

[S4] N. F. Mott and R. W. Gurney, Electronic Processes in Ionic Crystals, 1st ed, Oxford University Press, 1940.

[S5] P. N. J. Murgatroy, *J. Phys. D*: *Appl. Phys.*, 1970, **3**, 151.

[S6] A. Klant, C. Moya and J. Palomar, *J. Chem. Theory Comput.*, 12015, **11**, 4220.

[S7] A. D. Becke, *J. Chem. Phys.*, 1993, **98**, 1372.

[S8] M. A. Rohrdanz, K. M. Martins and J. M. Herbert, *J. Chem. Phys.*, 2009, **130**, 054112.

[S9] A. D, Boese and J. M. L. Martin, *J. Chem. Phys.*, 2004, **121**, 3405.

[S10] R. A. Marcus, *Rev. Mod. Phys.*, 1993, **65**, 599.

[S11] B. T. Thole, *Chem. Phys.*, 1981, **59**, 341.

[S12] J. Kirkpatrick, *Int. J. Quantum Chem.*, 2008, **108**, 51.

[S13] I. Yavuz, J. B. Lin and K. N. Houk, *Phys. Chem. Chem. Phys.*, 2019, **21**, 901.

[S14] V. Rühle, A. Lukyanov, F. May, M. Schrader, T. Vehoff, J. Kirkpatrick, B. Baumeier and D. Andrienko, *J. Chem. Theory Comput.*, 2011, **7**, 3335.

[S15] Materials Studio, Accelrys Software, Inc, San Diego, CA, 2014.

[S16] H. Sun, Z. Jin, C. Yang, R. L. C. Akkermans, S. H. Robertson, N. A. Spenley, S. Miller and S. M. Todd, *J Mol. Model.*, 2016, **22**, 47.

[S17] J. Salbeck, N. Yu, J. Bauer, F. Weissörtel and H. Bestgen, *Synth. Met.*, 1997, **91**, 209.

[S18] K. Rakstys, M. Saliba, P. Gao, P. Gratia, E. Kamarauskas, S. Paek, V. Jankauskas and M. K. Nazeeruddin, *Angew. Chem. Int. Ed.*, 2016, **55**, 7464.

[S19] M. Ren, J. Wang, X. Xie, J. Zhang and P. Wang, *ACS Energy Lett.*, 2019, **4**, 2683.